

Inversion doublets of reflection-asymmetric clustering in ^{28}Si and their isoscalar monopole and dipole transitions

Y. Chiba

Department of Physics, Hokkaido University, 060-0810 Sapporo, Japan

Y. Taniguchi

*Faculty of Health Sciences, Nihon Institute of Medical Science,
Moroyama, Saitama 350-0435, Japan*

M. Kimura

*Department of Physics, Hokkaido University, 060-0810 Sapporo, Japan and
Nuclear Reaction Data Centre, Faculty of Science,
Hokkaido University, Sapporo 060-0810, Japan*

(Dated: August 23, 2021)

Abstract

Background: Various cluster states of astrophysical interest are expected to exist in the excited states of ^{28}Si . However, they have not been identified firmly, because of the experimental and theoretical difficulties.

Purpose: To establish the $^{24}\text{Mg}+\alpha$, $^{16}\text{O}+^{12}\text{C}$ and $^{20}\text{Ne}+2\alpha$ cluster bands, we theoretically search for the negative-parity cluster bands that are paired with the positive-parity bands to constitute the inversion doublets. We also offer the isoscalar monopole and dipole transitions as a promising probe for the clustering. We numerically show that these transition strengths from the ground state to the cluster states are very enhanced.

Method: The antisymmetrized molecular dynamics with Gogny D1S effective interaction is employed to calculate the excited states of ^{28}Si . The isoscalar monopole and dipole transition strengths are directly evaluated from wave functions of the ground and excited states.

Results: Negative-parity bands having $^{24}\text{Mg}+\alpha$ and $^{16}\text{O}+^{12}\text{C}$ cluster configurations are obtained in addition to the newly calculated $^{20}\text{Ne}+2\alpha$ cluster bands. All of them are paired with the corresponding positive-parity bands to constitute the inversion doublets with various cluster configurations. The calculation show that the band-head of the $^{24}\text{Mg}+\alpha$ and $^{20}\text{Ne}+2\alpha$ cluster bands are strongly excited by the isoscalar monopole and dipole transitions.

Conclusions: The present calculation suggests the existence of the inversion doublets with the $^{24}\text{Mg}+\alpha$, $^{16}\text{O}+^{12}\text{C}$ and $^{20}\text{Ne}+2\alpha$ configurations. Because of the enhanced transition strengths, we offer the isoscalar monopole and dipole transitions as good probe for the $^{24}\text{Mg}+\alpha$ and $^{20}\text{Ne}+2\alpha$ cluster bands.

I. INTRODUCTION

Compared to light p -shell nuclei where the α clustering is prominent in the ground and excited states [1], the structure of the sd -shell nuclei is more complicated but much richer. The formation of the mean-field in the low-lying states, and its coexistence and mixing with the α , Carbon and Oxygen clustering yield various kinds of nuclear structures [2–4]. ^{28}Si is a typical example in the mid sd -shell nuclei. Its ground-state band has oblate deformed mean-field structure, while the rotational band built on the 0_3^+ state is prolately deformed suggesting the shape coexistence [5–8]. It is believed that the β vibration of the ground-state band yields another rotational band built on the 0_2^+ state [5, 8]. Furthermore, the possible existence of the superdeformed (SD) state is predicted by theoretical studies [4, 9–13] and the experimental candidates were observed [14–17].

In addition to these mean-field dynamics, ^{28}Si offers a rich variety of clustering. Many candidates of $^{24}\text{Mg} + \alpha$ cluster states are observed at more than 10 MeV above the ground state [18–22]. The existence of the $^{12}\text{C} + ^{16}\text{O}$ molecular resonance above $E_x \simeq 30$ MeV is also well known [23–29]. In addition to these highly excited cluster states, the possible clustering of the above-mentioned low-lying mean-field states has attracted many interests and has long been discussed [4, 12, 30–33]. For example, by the antisymmetrized molecular dynamics (AMD) study [4], it was pointed out that the ground-state band and SD band have large overlap with the $^{24}\text{Mg} + \alpha$ cluster configurations, while the prolate band largely overlaps with the $^{12}\text{C} + ^{16}\text{O}$ configuration. A similar discussion was also made by the algebraic cluster model [9, 13, 34, 35]. It is also noted that the α and Carbon cluster states at their decay thresholds are of astrophysical interest and importance, because they are closely related to and seriously affect to the stellar processes such as the He- and C-burning. Thus, the clustering phenomena in ^{28}Si is rich in variety and has scientific importance.

Despite of these strong interest and the continuous experimental and theoretical efforts, the clustering systematics in ^{28}Si is still ambiguous. Theoretically, the description of various kinds of cluster configurations within a single theoretical framework is not easy. In particular, the coexistence and mixing of mean-field and cluster configurations makes the theoretical description hard, although it enriches the clustering phenomena in ^{28}Si . Experimentally, the direct production of the cluster states by the transfer and radiative capture reactions are difficult, because of their small cross sections and very high level density. These difficulties

prevent us from the understanding and establishment of the clustering systematics in ^{28}Si .

To overcome these difficulties, we present the result of the AMD calculation to illustrate the clustering systematics and suggest the isoscalar (IS) monopole and dipole transitions as promising probe for clustering. We focus on the following two points. The first is the negative-parity cluster bands and the identification of the inversion doublets. The previous AMD study [4] investigated the structure of the positive-parity bands, and found that three positive-parity bands, the ground-state, prolate deformed and SD bands, have large overlap with the triaxial deformed $^{24}\text{Mg} + \alpha$, the $^{16}\text{O} + ^{12}\text{C}$ and the axially symmetric $^{24}\text{Mg} + \alpha$ cluster configurations, respectively. If these bands really have clustering aspects, they must be accompanied by the negative-parity bands to constitute the inversion doublets, because of their reflection-asymmetric intrinsic configurations [36]. Therefore, the identification of the inversion doublet is rather essential to establish the clustering systematics in ^{28}Si , and in this study, we extend our survey to the negative-parity states in this study.

The second is the IS monopole and dipole transitions which are expected to strongly populate the cluster inversion doublets. In this decade, the IS monopole transition attracts much interest as a good probe for the 0^+ cluster states [37–42]. In addition to this, recently, it was also suggested that the IS dipole transition is a good probe for the 1^- cluster states [43]. Therefore, the combination of the IS monopole and dipole transitions is expected to be a powerful tool to identify the inversion doublets mentioned above. Indeed, in Refs. [40, 43], by assuming that the ground states is a pure $SU(3)$ shell model state [44, 45] and the excited states are ideal cluster states, it was analytically proved that the IS monopole and dipole transition from the ground state to the excited cluster states are as strong as the single-particle estimates. However, in reality, the ground state of ^{28}Si deviates from a pure $SU(3)$ shell model state because of the strong influence of the spin-orbit interaction. Furthermore, in the excited states, the cluster configurations are mixed with the mean-field configurations. Therefore, the numerical calculations by the reliable nuclear models are indispensable for the quantitative discussions.

In this paper, we show that the various kinds of the cluster bands including the newly found $^{20}\text{Ne} + ^8\text{Be}$ band appear in the negative-parity and paired with the positive-parity bands to constitute the inversion doublets. The analysis of the wave function shows that the ground state has the duality of oblate deformed mean-field and the clustering of $^{24}\text{Mg} + \alpha$ and $^{20}\text{Ne} + ^8\text{Be}$ despite of the strong influence of the spin-orbit interaction. Because of

this duality, by the IS monopole and dipole transitions, the inversion doublets having the $^{24}\text{Mg} + \alpha$ and $^{20}\text{Ne} + ^8\text{Be}$ configurations are excited as strong as the single-particle estimates. Hence, it is concluded that the IS monopole and dipole transitions are regarded as promising probe for these clustering.

This article is organized as follows. In the next section, the framework of AMD is briefly explained. The cluster S -factor is also introduced as a measure of the clustering in the ground and excited states. In the Sec. III, the intrinsic wave function obtained by the energy variation and the energy spectrum are presented. The systematics of the clustering in ^{28}Si is summarized. The relationship between the clustering in the excited states and the IS monopole and dipole transitions is discussed in the Sec. IV. The final section summarizes this work.

II. FRAMEWORK

Here, the framework of AMD is briefly explained, and readers are directed to Refs. [46–48] for the detailed explanation.

A. Hamiltonian and variational wave function

The A -body microscopic Hamiltonian used in this study reads,

$$H = \sum_i^A t_i - t_{c.m.} + \sum_{i<j}^A v_{ij}^{NN} + \sum_{i<j}^A v_{ij}^{Coul}. \quad (1)$$

Here, t_i is kinetic energy of i -th nucleon. $t_{c.m.}$ is the center-of-mass kinetic energy which is exactly subtracted without approximation in the AMD framework. We employ Gogny D1S interaction [49] as an effective nuclear interaction v^{NN} . The Coulomb interaction v^{Coul} is approximated by a sum of seven Gaussians.

The intrinsic wave function of AMD is an antisymmetrized product of nucleon wave packets φ_i ,

$$\Phi_{int} = \mathcal{A} \{ \varphi_1 \varphi_2 \cdots \varphi_A \}, \quad (2)$$

where the nucleon wave packet is a direct product of the deformed Gaussian spatial part,

spin (χ_i) and isospin (ξ_i) parts,

$$\varphi_i(\mathbf{r}) = \phi_i(\mathbf{r})\chi_i\xi_i, \quad (3)$$

$$\phi_i(\mathbf{r}) = \exp\left\{-\sum_{\sigma=x,y,z} \nu_\sigma \left(r_\sigma - \frac{Z_{i\sigma}}{\sqrt{\nu_\sigma}}\right)^2\right\}, \quad (4)$$

$$\chi_i = a_i\chi_\uparrow + b_i\chi_\downarrow, \quad \xi_i = \text{proton or neutron.}$$

The centroids of the Gaussian wave packet \mathbf{Z}_i , the direction of nucleon spin a_i, b_i , and the width parameter of the deformed Gaussian ν_σ are the variational parameters [3].

Before the energy variation, the intrinsic wave function is projected to the eigenstates of the parity,

$$\Phi^\pi = \frac{1 + \pi P_x}{2} \Phi_{int}, \quad \pi = \pm. \quad (5)$$

Using this wave function, the variational energy is defined as,

$$E^\pi = \frac{\langle \Phi^\pi | H | \Phi^\pi \rangle}{\langle \Phi^\pi | \Phi^\pi \rangle} + V_c. \quad (6)$$

By the frictional cooling method, above-mentioned variational parameters are determined so that E^π is minimized. Here V_c is the potential which imposes the constraint on the variational wave function. In this study, we introduce two different constraint potentials. The first is the $\beta\gamma$ -constraint which is imposed on the quadrupole deformation of the variational wave function,

$$V_c = v_\beta(\langle \beta \rangle - \beta_0)^2 + v_\gamma(\langle \gamma \rangle - \gamma_0)^2, \quad (7)$$

where $\langle \beta \rangle$ and $\langle \gamma \rangle$ are the quadrupole deformation parameters of the intrinsic wave function defined in Ref. [50], and v_β and v_γ are chosen large enough that $\langle \beta \rangle$ and $\langle \gamma \rangle$ are close to β_0 and γ_0 after the frictional cooling.

Another constraint is d -constraint [51] which is imposed on the distance between *quasi clusters*,

$$V_c = v_d(\langle d^2 \rangle - d_0^2)^2. \quad (8)$$

Similar to the $\beta\gamma$ -constraint, v_d is chosen so that the squared distance between quasi clusters $\langle d^2 \rangle$ is close to d_0^2 after the frictional cooling. The squared distance between quasi clusters is defined as follows. First, we select nucleons which belongs to each quasi cluster. For

example, in the case of the $\alpha + {}^{24}\text{Mg}$ configuration, we choose 4 nucleon wave packets which belong to α cluster and regard remaining 24 wave packets as belonging to ${}^{24}\text{Mg}$ cluster. Then, we define the center-of-mass of these quasi-clusters as

$$\mathbf{R}_\alpha = \frac{1}{4} \sum_{i \in \alpha} \mathfrak{R}(\mathbf{Z}_i), \quad \mathbf{R}_{24\text{Mg}} = \frac{1}{24} \sum_{i \in 24\text{Mg}} \mathfrak{R}(\mathbf{Z}_i), \quad (9)$$

and define $\langle d^2 \rangle$ as the squared distance between those centers-of-mass,

$$\langle d^2 \rangle = |\mathbf{R}_\alpha - \mathbf{R}_{24\text{Mg}}|^2. \quad (10)$$

Then we find the wave function which yields the minimum energy for given value of $\langle d^2 \rangle$ by the energy minimization. By applying this constraint, various kinds of cluster configurations have been studied [4, 51–53]. In the present study, we calculated $\alpha + {}^{24}\text{Mg}$, ${}^{12}\text{C} + {}^{16}\text{O}$ and ${}^8\text{Be} + {}^{16}\text{O}$ cluster configurations. It is noted that the d -constraint imposes the constraint on the distance between the quasi clusters, but do not on their internal structure. As a result, when the inter-cluster distance is small, the clusters are strongly polarized to gain more binding energy. On the other hand, when the distance is sufficiently large, the clusters are in their ground states. In other words, this constraint smoothly connects the mean-field and cluster states as function of the inter-cluster distance.

In the following, for the sake of the simplicity, we denote the set of the wave functions obtained by the above-mentioned constrained energy variations as Φ_i^π where the subscript i is the index for each wave function. They are used as the basis wave functions for GCM calculation explained below.

B. Angular momentum projection and generator coordinate method

After the energy variation, we project the wave function to the eigenstate of the angular momentum.

$$\Phi_{MKi}^{J\pi} = n \frac{2J+1}{8\pi^2} \int d\Omega D_{MK}^{J*}(\Omega) R(\Omega) \Phi_i^\pi, \quad (11)$$

where n , $D_{MK}^J(\Omega)$ and $R(\Omega)$ are the normalization factor, Wigner's D function and the rotation operator, respectively. Then, they are superposed to describe the eigenstates of

Hamiltonian,

$$\Psi_n^{J\pi} = \sum_{Ki} c_{Kin} \Phi_{MKi}^{J\pi} \quad (12)$$

The coefficient c_{Kin} is determined by solving Hill-Wheeler equation (GCM) [54, 55],

$$\begin{aligned} & \sum_{K'j} \langle \Phi_{MKi}^{J\pi} | H | \Phi_{MK'j}^{J\pi} \rangle c_{K'jn} \\ &= E_n \sum_{K'j} \langle \Phi_{MKi}^{J\pi} | \Phi_{MK'j}^{J\pi} \rangle c_{K'jn}. \end{aligned} \quad (13)$$

In the following, we call thus-obtained wave function GCM wave function.

In general, a GCM wave function given by Eq. (12) is a mixture of various cluster and non-cluster configurations. Therefore, we introduce two measures to identify cluster states from the results of GCM calculations. The first measure is the overlap between the GCM wave function and the basis wave function,

$$O_i = |\langle \Psi_n^{J\pi} | \Phi_i^{J\pi} \rangle|^2. \quad (14)$$

If the overlap O_i with a certain $\Phi_i^{J\pi}$ is sufficiently large, the state described by $\Psi_n^{J\pi}$ may be interpreted to have the cluster configuration described by $\Phi_i^{J\pi}$.

To define more quantitative measure, we introduce the projector to the cluster subspace. For example, the projector to the subspace spanned by the $^{16}\text{O} + ^{12}\text{C}$ configurations cluster is defined as

$$P_{^{16}\text{O}+^{12}\text{C}} = \sum_i |\Phi_{^{16}\text{O}+^{12}\text{C}}^{J\pi}(d_j)\rangle B_{ij}^{-1} \langle \Phi_{^{16}\text{O}+^{12}\text{C}}^{J\pi}(d_i)|, \quad (15)$$

$$B_{ij} = \langle \Phi_{^{16}\text{O}+^{12}\text{C}}^{J\pi}(d_i) | \Phi_{^{16}\text{O}+^{12}\text{C}}^{J\pi}(d_j) \rangle. \quad (16)$$

Here, $|\Phi_{^{16}\text{O}+^{12}\text{C}}^{J\pi}(d)\rangle$ denote the wave functions having $^{16}\text{O} + ^{12}\text{C}$ cluster configurations with inter-cluster distance d obtained by applying the d -constraint. The expectation value of $P_{^{16}\text{O}+^{12}\text{C}}$, which we call cluster S -factor in the following, is a good measure to know to what extent a GCM wave function is inside of the $^{16}\text{O} + ^{12}\text{C}$ cluster subspace;

$$S_{^{16}\text{O}+^{12}\text{C}} = \langle \Psi_n^{J\pi} | P_{^{16}\text{O}+^{12}\text{C}} | \Psi_n^{J\pi} \rangle. \quad (17)$$

The cluster S -factors for $^{24}\text{Mg} + \alpha$, $^{20}\text{Ne} + ^8\text{Be}$ and $^{16}\text{O} + ^{12}\text{C}$ configurations are also defined in the same manner. As already explained above, when the inter-cluster distance d is too small, the wave function obtained by the d -constraint do not have cluster structure. Therefore, we use the wave functions having non-small inter-cluster distance ($d \geq 4.0$ fm) to define the projectors.

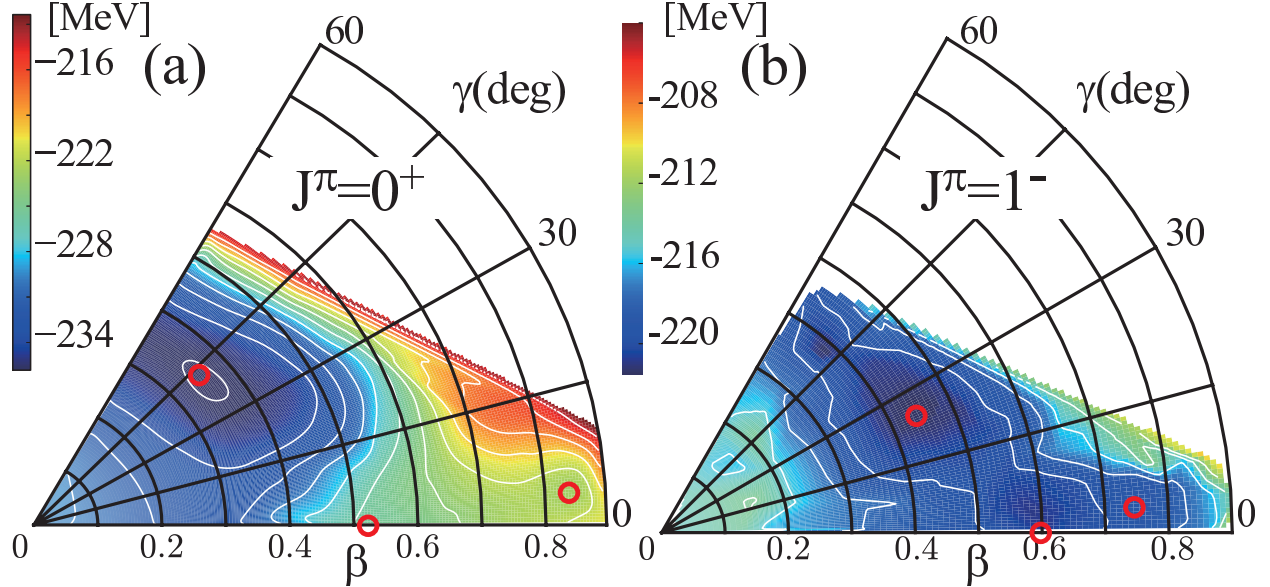


FIG. 1. (Color online) The energy surfaces as functions of the quadrupole deformation parameters β and γ obtained by the energy variation with $\beta\gamma$ -constraint and the angular momentum projection to the (a) $J^\pi = 0^+$ and (b) $J^\pi = 1^-$. Red circles show the energy minima or plateau.

III. RESULTS AND DISCUSSIONS

A. Result of energy variation

The energy surface of the $J^\pi = 0^+$ state obtained by the $\beta\gamma$ constraint and the angular momentum projection is shown in Fig. 1 (a). There exist a couple of energy minima or plateau with different quadrupole deformations. The lowest energy minimum has an oblate shape of $(\beta, \gamma) = (0.36, 46^\circ)$ with the energy $E = -235.7$ MeV, whose intrinsic density distribution is shown in Fig. 2 (a). Around this global minimum, the energy surface is rather soft against both of β and γ deformation. The second lowest state is prolately deformed as seen in its intrinsic density distribution (Fig. 2 (b)) and locates at $(\beta, \gamma) = (0.5, 0^\circ)$ as a very shallow energy minimum. Those two energy minima indicate the oblate and prolate shape coexistence in this nucleus and yield the oblate deformed ground state and the prolate deformed 0_3^+ state by the GCM calculation, respectively. By further increase of the deformation, the third energy minimum with strongly elongated shape (Fig. 2 (c)) appears at $(\beta, \gamma) = (0.85, 5^\circ)$. As discussed in Ref. [4], this configuration has the a $(sd)^8(pf)^4$ configuration and becomes the dominant component of the 0_4^+ state which is regarded as

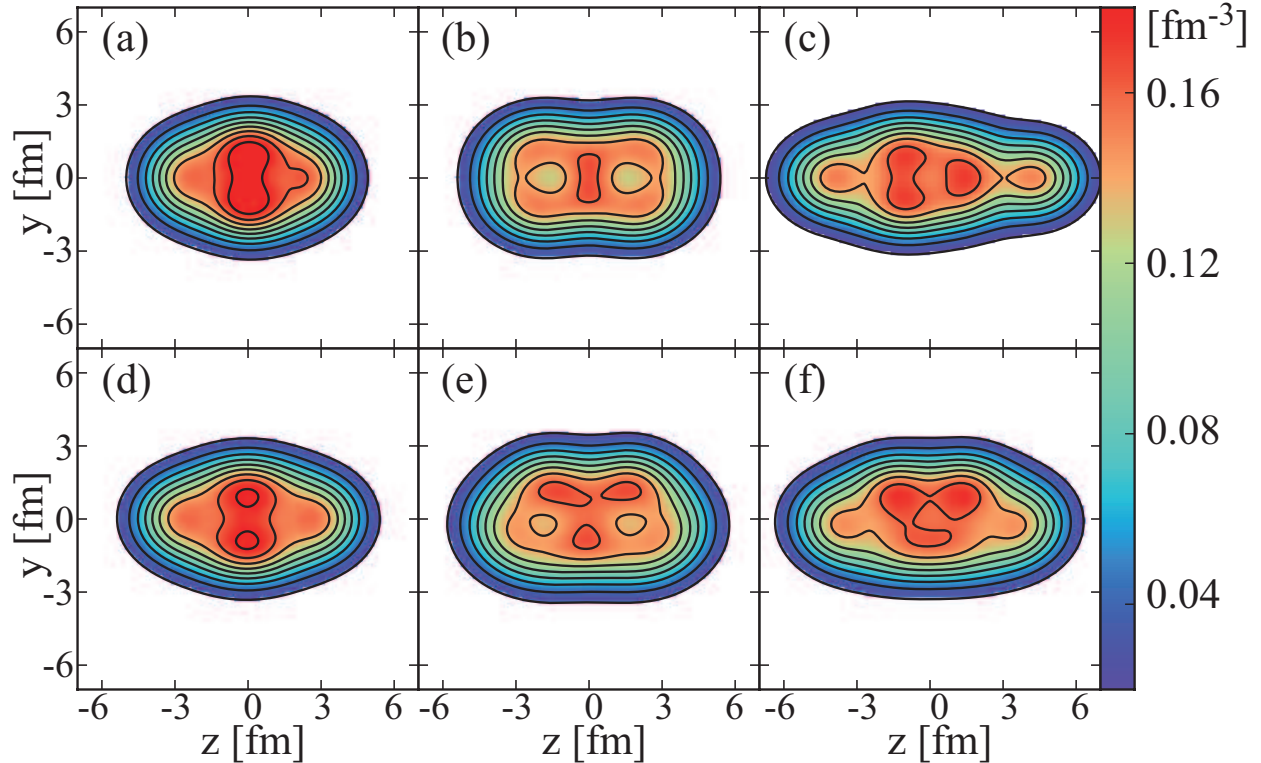


FIG. 2. (Color online) Intrinsic matter density distributions of the minima on the positive- and negative-parity energy surfaces obtained by $\beta\gamma$ -constraint shown in Fig. 1. The panels (a), (b) and (c) show the oblate, prolate and SD $J^\pi = 0^+$ minima, while the panels (d), (e) and (f) show the $J^\pi = 1^-$ minima generated by the $1p1h$ excitations from the positive-parity minima.

the SD state.

The energy surface of the negative-parity $J^\pi = 1^-$ state shown in Fig. 1 (b) does not have clear local minima, but there are three shallow minima or plateau that are generated by the single-particle excitations. The global minimum is located at $(\beta, \gamma) = (0.43, 27^\circ)$ with the energy $E = -221.2$ MeV. This configuration has the density distribution (Fig. 2 (d)) similar to the oblate deformed ground state, because it is generated by the one-nucleon excitation from the ground state configuration. As shown in Fig. 2 (e) and (f), there also exist the prolate deformed and SD negative-parity minima that are generated by the $1p1h$ excitations from the corresponding positive-parity minima. They are respectively located at $(\beta, \gamma) = (0.60, 0^\circ)$ and $(0.73, 2^\circ)$ with the energies $E = -220.8$ and -219.1 MeV. In terms of the Nilsson orbit, the prolate minimum is generated by the nucleon excitation from the $[Nn_z m_l \Omega^\pi] = [211 1/2^+]$ orbit to the $[330 1/2^-]$ orbit, while the negative-parity SD minimum

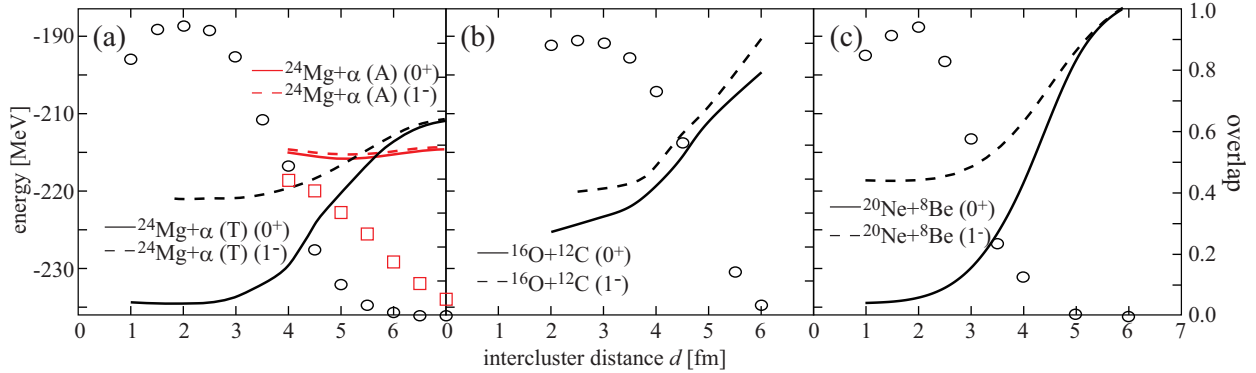


FIG. 3. Energy curves obtained by d -constraint. Panels (a), (b) and (c) respectively show the energy curves of the $J^\pi = 0^+$ and 1^- states having $^{24}\text{Mg} + \alpha$, $^{16}\text{O} + ^{12}\text{C}$ and $^{20}\text{Ne} + ^8\text{Be}$ configurations. Circles and Boxes in the figure show the overlap between these $J^\pi = 0^+$ cluster configurations and the energy minima on the $\beta\gamma$ energy surface. Black circles in panels (a) and (c) shows the overlap between the oblate deformed minimum (ground state) and $^{24}\text{Mg} + \alpha(\text{T})$, $^{20}\text{Ne} + ^8\text{Be}$ cluster configurations, while the red boxes in the panel (a) show the overlap between the SD minimum and $^{24}\text{Mg} + \alpha(\text{A})$ configuration. The circles in the panel (b) show the overlap between the prolate deformed minimum and the $^{12}\text{C} + ^{16}\text{O}$ configuration.

is generated by the nucleon deexcitation from the $[330\ 1/2^-]$ orbit to the $[211\ 1/2^+]$ orbit.

As confirmed from the intrinsic density distributions shown in Fig. 2, the energy variation with the $\beta\gamma$ constraint does not generate prominent cluster configurations, but mean-field configurations. On the other hand, the d -constraint yields various cluster configurations. Figure 3 shows the energy curves obtained by the d -constraint. In the previous study, the d -constraint method was applied to the positive-parity states of the $^{24}\text{Mg} + \alpha$ and the $^{16}\text{O} + ^{12}\text{C}$ configurations. In addition to them, in the present study, we applied it to the $^{20}\text{Ne} + ^8\text{Be}$ configuration and investigated both of the positive- and negative-parity. As a result, we found that all of these cluster configurations appear in both parity states.

Figure 3 (a) shows the energy curves for $^{24}\text{Mg} + \alpha$ cluster configurations projected to the $J^\pi = 0^+$ and 1^- states. Because ^{24}Mg cluster is prolately deformed, two different $^{24}\text{Mg} + \alpha$ configurations were obtained, in which the orientations of ^{24}Mg cluster are different. In the configuration denoted by $^{24}\text{Mg} + \alpha(\text{T})$, the longest axis of ^{24}Mg is perpendicular to the

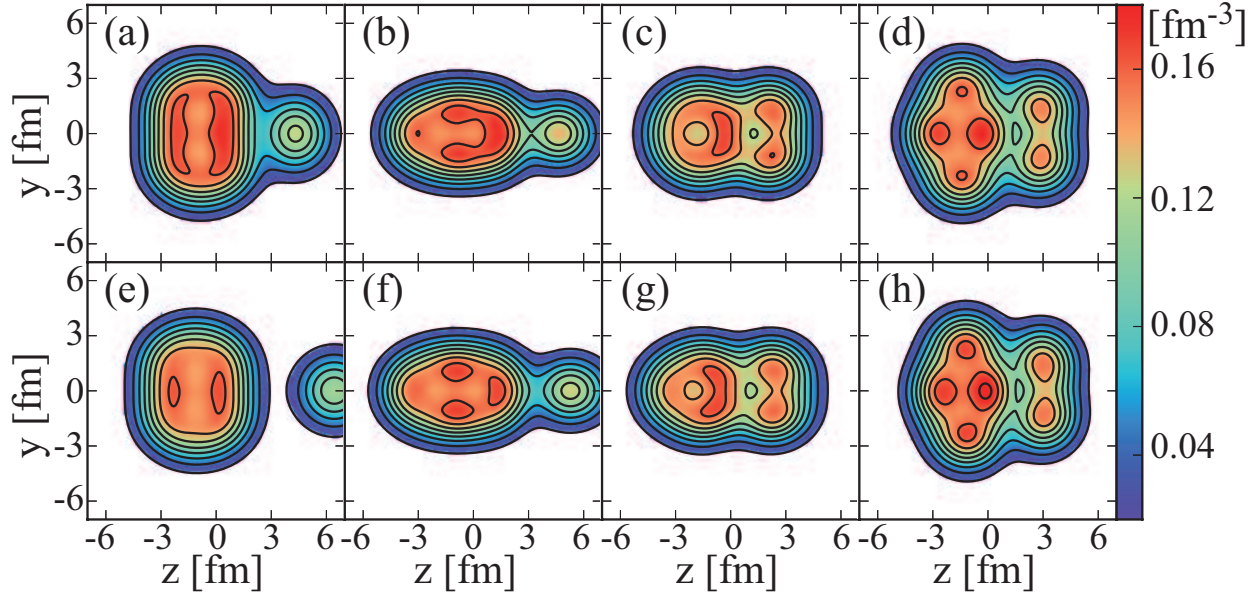


FIG. 4. (Color online) Intrinsic matter density distributions obtained by d -constraint. (a), (b), (c) and (d) respectively show the $^{24}\text{Mg} + \alpha$ (T), $^{24}\text{Mg} + \alpha$ (A), $^{16}\text{O} + ^{12}\text{C}$ and $^{20}\text{Ne} + ^8\text{Be}$ configurations with $J^\pi = 0^+$, while (e), (f), (g) and (h) show the $J^\pi = 1^-$ partner having the same configurations.

inter-cluster coordinate between ^{24}Mg and α clusters. As a result, total system is triaxially deformed as seen in its density distribution shown in Fig. 4 (a). It is noted that, when the inter-cluster distance becomes small, the wave function of this configuration with $J^\pi = 0^+$ becomes almost identical to that of the oblate minimum on the $\beta\gamma$ energy surface (*i.e.* the ground state). The overlap between the wave functions of the $^{24}\text{Mg} + \alpha$ (T) configuration and the oblate deformed ground state minimum (circles in Fig. 3 (a)) has the maximum value 0.96 at $d = 2.0$ fm, and their energies are very close to each other (-235.7 MeV and -234.5 MeV, respectively). Note that it does not necessarily mean that the ground state is clustered, but it means the equivalence of the cluster and shell model wave functions at small inter-cluster distance. This duality of shell and cluster is an essential ingredient for the enhanced monopole and dipole transitions discussed in the section IV.

The negative-parity $J^\pi = 1^-$ state with the same $^{24}\text{Mg} + \alpha$ (T) configuration (Fig. 4 (e)) appears at relatively high excitation energy that is approximately 15 MeV above the ground state. Different from the $J^\pi = 0^+$ state, this negative-parity state has small overlap with the negative-parity minima in the $\beta\gamma$ energy surface, which amount to 0.20 at most. Other cluster configurations mentioned below also have small overlap with the mean-

field configurations. This means that the $\beta\gamma$ constraint and d -constraint are describing the different class of the negative-parity states. Namely, the $\beta\gamma$ constraint yields the single-particle excited states built on the mean-field, while the d -constraint yields the reflection-asymmetric cluster states in which the relative motion between clusters have odd angular momenta.

In another $^{24}\text{Mg} + \alpha$ configuration denoted by $^{24}\text{Mg} + \alpha$ (A), the longest axis of the ^{24}Mg cluster is parallel to the inter-cluster coordinate, and hence, the system is axially deformed as shown in Fig. 4 (b). This configuration with $J^\pi = 0^+$ has large overlap with the SD configuration shown in Fig. 2 (c). The overlap between them amounts to 0.42 at the inter-cluster distance $d = 4.5$ fm. It is interesting to note that the negative-parity $J^\pi = 1^-$ state (Fig. 4 (f)) has almost the same intrinsic density distribution and almost the same energy with the positive-parity $J^\pi = 0^+$ state. It is because of the large inter-cluster distance of the $^{24}\text{Mg} + \alpha$ (A) configuration compared to the $^{24}\text{Mg} + \alpha$ (T) configuration. The $^{24}\text{Mg} + \alpha$ (A) configuration in negative-parity does not have corresponding state on $\beta\gamma$ energy surface having large overlap.

The $^{16}\text{O} + ^{12}\text{C}$ configuration with $J^\pi = 0^+$ appears approximately 10 MeV above the ground state with the inter-cluster distance $d = 2.5$ fm. At small inter-cluster distance, this configuration has large overlap with the prolate minimum located at $(\beta, \gamma) = (0.5, 0^\circ)$ on the $\beta\gamma$ energy surface (Fig. 2 (c)). The overlap amounts to 0.90 at $d = 2.5$ fm. The negative-parity $J^\pi = 1^-$ state has similar intrinsic density distribution to the positive-parity state as shown in Fig. 4 (g) and has the excitation energy close to its positive-parity partner. We also obtained another $^{16}\text{O} + ^{12}\text{C}$ configuration having different orientation of the ^{12}C which may corresponds the highly excited $^{16}\text{O} + ^{12}\text{C}$ cluster states or molecular resonances [23–29]. However, its energy is rather high and is not discussed here. Finally, we explain the $^{20}\text{Ne} + ^8\text{Be}$ configuration. It has the triaxial intrinsic density distribution as shown in Fig. 4 (d) in which the longest axes of ^{20}Ne and ^8Be clusters are parallel to each other, but perpendicular to the inter-cluster coordinate. At small inter-cluster distance, this configuration with $J^\pi = 0^+$ becomes identical to the oblate minimum on $\beta\gamma$ energy surface (the ground state). Thus, the ground state, the $^{24}\text{Mg} + \alpha$ and $^{20}\text{Ne} + ^8\text{Be}$ cluster configurations have large overlap to each other at small inter-cluster distance. The negative-parity $J^\pi = 1^-$ state of $^{20}\text{Ne} + ^8\text{Be}$ configuration appears at approximately 17 MeV above the ground state with the inter-cluster distance $d = 3.0$ fm.

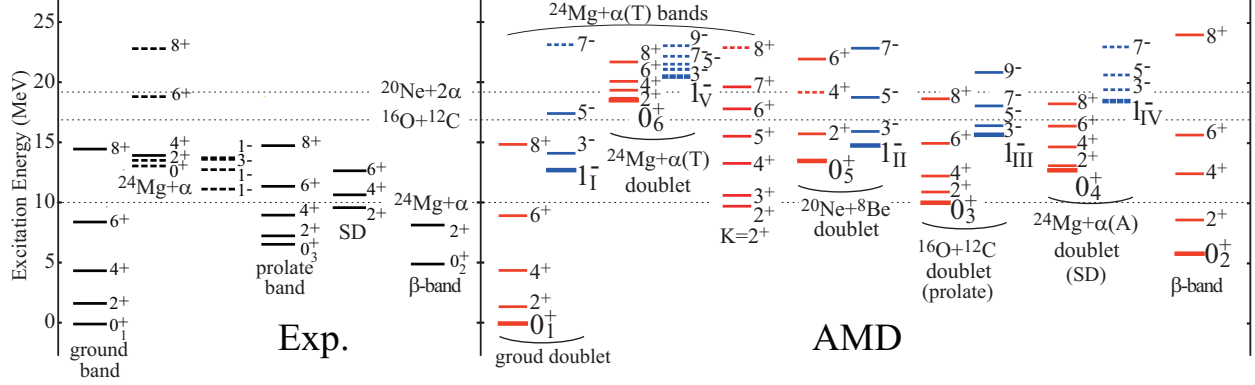


FIG. 5. Calculated and observed partial level scheme of ^{28}Si . The levels shown by dashed lines are the averaged energies of the several states which have sizable cluster S -factors. Dotted lines show the $^{24}\text{Mg} + \alpha$, $^{16}\text{O} + ^{12}\text{C}$ and $^{20}\text{Ne} + 2\alpha$ threshold energies.

The result of the energy variation is summarized as follows. (1) The $\beta\gamma$ constraint yielded three mean-field configurations with $J^\pi = 0^+$ having oblate, prolate and SD shapes. The oblate minimum has the lowest energy and corresponds to the ground state, while the others constitute the excited 0^+ states. (2) The d -constraint yielded prominent $^{24}\text{Mg} + \alpha$ (T) and (A), $^{16}\text{O} + ^{12}\text{C}$ and $^{20}\text{Ne} + ^8\text{Be}$ cluster configurations with large inter-cluster distance and smoothly connects them to the mean-field states at small inter-cluster distance. These cluster configurations have large overlap with the mean-field configurations indicating that the prolate, oblate and SD minima on $\beta\gamma$ energy surface have duality of shell and cluster. Namely, the oblate deformed ground state has the duality of $^{24}\text{Mg} + \alpha$ (T) and $^{20}\text{Ne} + ^8\text{Be}$ cluster configurations. The prolate minimum has the duality of the $^{16}\text{O} + ^{12}\text{C}$ configuration and the SD minimum has the duality of the $^{24}\text{Mg} + \alpha$ (A) configuration. (3) All of the cluster configurations are accompanied by the negative-parity partner having almost the same intrinsic density distributions. These negative-parity states originate in their reflection-asymmetric cluster configurations.

B. Excitation spectrum and clustering

1. Overview of the spectrum

Figure 5 shows the energy levels obtained by the GCM calculation together with the corresponding observed states. In the figure, the rotational bands which have sizable amount

of the cluster S -factors and overlaps with the cluster wave functions are shown. Other excited states are omitted except for the β -band built on the ground-state band. The detailed distribution of the cluster S -factors in the excited states is discussed in the section IV.

The results for the positive-parity states are consistent with our previous study, and we find that the most of the positive-parity bands are accompanied by the negative-parity bands because of their duality of mean-field and reflection-asymmetric clustering. The present result is briefly summarized as follows. The oblate minimum on the $\beta\gamma$ energy surface and the $^{24}\text{Mg} + \alpha$ (T) configuration are mixed to each other and generate a group of the rotational bands denoted by $^{24}\text{Mg} + \alpha$ (T) bands in Fig. 5. The oblate minimum also mixed with the $^{20}\text{Ne} + ^8\text{Be}$ configuration to generate a pair of the positive- and negative-parity bands denoted by $^{20}\text{Ne} + ^8\text{Be}$ doublet. In a similar way, the prolate deformed minimum is mixed with the $^{16}\text{O} + ^{12}\text{C}$ configuration, and the SD minimum is mixed with the $^{24}\text{Mg} + \alpha$ (A) configuration. As a result, they respectively generate pairs of the positive- and negative-parity bands, which are denoted by $^{16}\text{O} + ^{12}\text{C}$ and $^{24}\text{Mg} + \alpha$ (A) doublets. In addition to them, the positive-parity band denoted by β -band is generated by the β vibration of the ground-state band.

2. $^{24}\text{Mg} + \alpha$ (T) bands

A group of the rotational bands denoted by $^{24}\text{Mg} + \alpha$ (T) bands includes three positive-parity bands and two negative-parity bands. The positive-parity bands are the ground-state band ($K^\pi = 0^+$), $K^\pi = 2^+$ band and another $K^\pi = 0^+$ band built on the 0_6^+ state at 18.2 MeV. Because of the reflection-asymmetric clustering of the $^{24}\text{Mg} + \alpha$ (T) configuration, two negative-parity $K^\pi = 0^-$ bands built on the 1_1^- and 1_{1V}^- are paired with the $K^\pi = 0^+$ bands to constitute two parity doublets which are denoted by the ground doublet and $^{24}\text{Mg} + \alpha$ (T) doublet in the figure.

The ground-state band is dominated by the oblately deformed mean-field configuration shown in Fig. 2 (a) whose overlap with the GCM wave function amounts to 0.84. The moment-of-inertia of the ground-state band and the $B(E2)$ strengths listed in Tab. I reasonably agree with the observed data, indicating that the deformed mean-field nature of the ground state is properly described by the present calculation. However, it must be noted that this ground-state band also has the large overlap with the $^{24}\text{Mg} + \alpha$ (T) configuration

TABLE I. The calculated in-band $B(E2)$ ($e^2\text{fm}^4$) strengths in the ground-state, $^{24}\text{Mg} + \alpha$ (T), $^{20}\text{Ne} + ^8\text{Be}$, $^{16}\text{O} + ^{12}\text{C}$, $^{24}\text{Mg} + \alpha$ (A) doublets and in the β -band. The numbers in the parenthesis are the experimental data [17].

	ground	$^{24}\text{Mg} + \alpha$ (T)	$^{20}\text{Ne} + ^8\text{Be}$
$B(E2; 2^+ \rightarrow 0^+)$	79.4 (67)	29.2	15.3
$B(E2; 4^+ \rightarrow 2^+)$	123 (83)	28.9	12.7
$B(E2; 3^- \rightarrow 1^-)$	94.9	24.9	18.3
$B(E2; 5^- \rightarrow 3^-)$	111	27.2	10.8
	$^{16}\text{O} + ^{12}\text{C}$	$^{24}\text{Mg} + \alpha$ (A)	β -band
$B(E2; 2^+ \rightarrow 0^+)$	221	664	52.8
$B(E2; 4^+ \rightarrow 2^+)$	299 (150)	939	69.7
$B(E2; 3^- \rightarrow 1^-)$	244	409	
$B(E2; 5^- \rightarrow 3^-)$	382	424	

with small inter-cluster distance, which amount to 0.96 for $d = 2.0$ fm. This means that the ground-state band has a duality of the oblate shaped mean-field and $^{24}\text{Mg} + \alpha$ (T) clustering. Therefore, the excitation of the inter-cluster motion between ^{24}Mg and α clusters yields excited bands with prominent clustering. The $1\hbar\omega$ excitation of the inter-cluster motion yields the $K^\pi = 0^-$ band built on the 1^- state denoted by 1_1^- which is dominated by the negative-parity $^{24}\text{Mg} + \alpha$ (T) configuration with $d = 2.5$ fm. Hence, we assigned it as the partner of the ground-state band which constitutes the ground doublet, although the $1p1h$ mean-field configuration (Fig. 2 (d)) also has non-negligible contribution to this band. In addition to the ground doublet, the 2 and $3\hbar\omega$ excitations of the inter-cluster motion yield $K^\pi = 0^\pm$ bands built on the 0_6^+ state and a group of 1^- states denoted by $1_{\bar{v}}^-$, which constitute another doublet denoted by $^{24}\text{Mg} + \alpha$ (T) doublet. Because of the coupling with other non-cluster configurations, three 1^- states around 22 MeV have large $^{24}\text{Mg} + \alpha$ cluster S -factors, and their averaged energy is denoted by $1_{\bar{v}}^-$ in Fig. 5. As the inter-cluster motion is largely excited, these bands have prominent cluster structure. The 0_6^+ and $1_{\bar{v}}^-$ states have large overlap with the configurations shown in Fig. 4 (a) and (e) which amount to 0.32 and 0.22 (averaged), respectively. In addition to these parity doublets, the triaxial deformation of the $^{24}\text{Mg} + \alpha$ (T) configuration yields $K^\pi = 2^+$ band. Thus, the duality of the ground

state yields two parity doublets and $K^\pi = 2^+$ band which are classified as $^{24}\text{Mg} + \alpha$ (T) bands.

3. $^{20}\text{Ne} + ^8\text{Be}$ doublet and β -band

As discussed in the section III A, the oblate deformed minimum also has large overlap with the $^{20}\text{Ne} + ^8\text{Be}$ configuration with small inter-cluster distance. Therefore, the excitation of the inter-cluster motion between ^{20}Ne and ^8Be clusters should yield a series of the cluster bands. In addition, the deformed mean-field aspect of the ground state can yield a different kind of excitation mode, *i.e.* the β vibration. The GCM calculation showed that these two excitation modes strongly mix to each other to yield the 0_2^+ and 0_5^+ states. Their overlap with the configurations shown in Fig. 4 (d) amount to 0.13 and 0.18, respectively. Similarly to the $^{24}\text{Mg} + \alpha$ configuration, the $^{20}\text{Ne} + ^8\text{Be}$ configuration yields the 1_{II}^- state which is paired with the 0_5^+ state to constitute the parity doublet denoted by $^{20}\text{Ne} + ^8\text{Be}$ doublet.

4. $^{16}\text{O} + ^{12}\text{C}$ doublet and $^{24}\text{Mg} + \alpha$ (A) doublet

In addition to the above-mentioned bands related to the ground state duality, there are other bands which are unrelated to the ground state. The prolate band is built on the 0_3^+ state at 10.0 MeV which has the large overlap with the prolate deformed local minimum shown in Fig. 2 (b). Combined with the oblately deformed ground state, this prolate deformed 0_3^+ state indicates the shape coexistence in the low-lying states of ^{28}Si . As discussed in the previous work [4], this prolate band has large overlap with the $^{16}\text{O} + ^{12}\text{C}$ cluster configuration. Hence, it is concluded that the prolate band has the duality of the prolate deformed mean-field and $^{16}\text{O} + ^{12}\text{C}$ clustering. The negative-parity band built on the 1_{III}^- state also has the large overlap with the $^{16}\text{O} + ^{12}\text{C}$ configuration (Fig. 4 (g)), and assigned as the partner of the positive-parity prolate band, that constitutes the $^{16}\text{O} + ^{12}\text{C}$ doublet.

Another prolate deformed minimum *i.e.* the SD minimum located at $(\beta, \gamma) = (0.85, 5^\circ)$ generates the SD band built on the 0_4^+ state at 12.7 MeV. This band has large overlap with the $^{24}\text{Mg} + \alpha$ (A) configuration shown in the Fig. 4 (f). There are two 1^- states having large overlap with the negative-parity $^{24}\text{Mg} + \alpha$ (A) configuration and the mixing with the

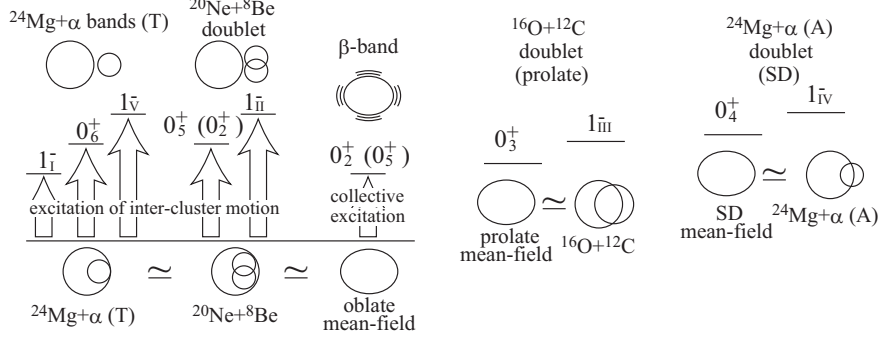


FIG. 6. The oblate deformed ground state has the duality of the mean field and $^{24}\text{Mg} + \alpha$ (T) and $^{16}\text{O} + ^{12}\text{C}$ clustering. From the duality, β -band, $^{24}\text{Mg} + \alpha$ bands and $^{20}\text{Ne} + ^8\text{Be}$ doublet arise.

$^{16}\text{O} + ^{12}\text{C}$ configuration. Their averaged energy is denoted by 1_{IV}^- and the negative-parity band built on these states is associated with the positive-parity band. We denote this doublet as $^{24}\text{Mg} + \alpha$ (A) doublet. As discussed in the previous section, the $^{16}\text{O} + ^{12}\text{C}$ and $^{24}\text{Mg} + \alpha$ (A) configurations do not have overlap with the oblate deformed ground state. Therefore, the $^{16}\text{O} + ^{12}\text{C}$ and $^{24}\text{Mg} + \alpha$ (A) doublets are disconnected with the ground state.

5. Systematics of clustering and observed candidates

To summarize this section, the systematics of the cluster states explained above is schematically illustrated in Fig. 6. The ground state has duality of the oblate deformed mean-field, $^{24}\text{Mg} + \alpha$ (T) and $^{20}\text{Ne} + ^8\text{Be}$ cluster configurations. By the excitation of the inter-cluster motion between ^{24}Mg and α clusters yields a group of the $^{24}\text{Mg} + \alpha$ (T) bands. The $^{20}\text{Ne} + ^8\text{Be}$ clustering also arise from the ground state duality and it is strongly mixed with the β -vibration mode which arises from the mean-field aspect of the ground state. Aside from these bands, the $^{16}\text{O} + ^{12}\text{C}$ and $^{24}\text{Mg} + \alpha$ (A) doublets exist and disconnected from the ground state, because of the orthogonality of their cluster configurations to the ground state.

Experimentally, the low-lying three positive-parity bands, *i.e.* the ground-state band, β -band and the prolate band, are assigned firmly and coincide with the present calculation, although the calculation slightly overestimates the energies of the excited bands. On the other hand, the experimental assignment of the negative-parity bands and high-lying bands are not established yet, and hence, the assignment of the cluster bands is still ambiguous.

Many experiments have been performed to identify the cluster bands [17–23, 29], and Fig. 5 shows the candidates of the cluster bands reported in Refs. [17, 19, 22], which energetically coincide with the present calculation. A couple of $0^+, 2^+$ and $1^-, 3^-$ states were reported around $E_x = 13$ MeV by the α transfer and radiative α capture reactions. They have relatively large α decay width, hence, can be regarded as the candidates of the $^{24}\text{Mg}+\alpha$ (T) or $^{24}\text{Mg}+\alpha$ (A) doublets. Furthermore, based on the analysis of the $^{24}\text{Mg}(\alpha, \gamma)$ and $^{12}\text{C}(^{20}\text{Ne}, \alpha)^{28}\text{Si}$ reactions, another rotational band was suggested [17] and the authors were assigned it to the SD band predicted by the previous AMD study [4].

IV. ISOSCALAR MONOPOLE AND DIPOLE TRANSITIONS

Here, we discuss that part of the clustering systematics summarized above can be detected by the IS monopole and dipole transitions from the ground state. To illustrate it, we first discuss the the duality of shell and cluster. Then, we present the result of AMD calculation to show that the IS monopole and dipole transitions strongly yield cluster states.

A. Duality of shell and cluster

In the section III, we have explained that the many low-lying positive-parity states have the duality of the mean-field (shell) and cluster. Here, we show that it is reasonably understood by the $SU(3)$ shell model [44, 45] and the Bayman-Bohr theorem [56, 57].

^{28}Si has 12 nucleons in sd -shell on top of the ^{16}O core and its oblate deformed ground state can be approximated by the $(\lambda, \mu) = (0, 12)$ representation of $SU(3)$ shell model. Denoting the eigenstates of three-dimensional harmonic oscillator in the Cartesian representation $(n_x n_y n_z)$, it is written as

$$(\lambda, \mu) = (0, 12) : (002)^4(011)^4(020)^4, \quad (18)$$

where the configuration of 12 nucleons are explicitly shown, and the ^{16}O core which corresponds to $(000)^4(100)^4(010)^4(001)^4$ is omitted. In a same manner, the prolate deformed state is approximated by the $(\lambda, \mu) = (12, 0)$ representation,

$$(\lambda, \mu) = (12, 0) : (002)^4(011)^4(101)^4, \quad (19)$$

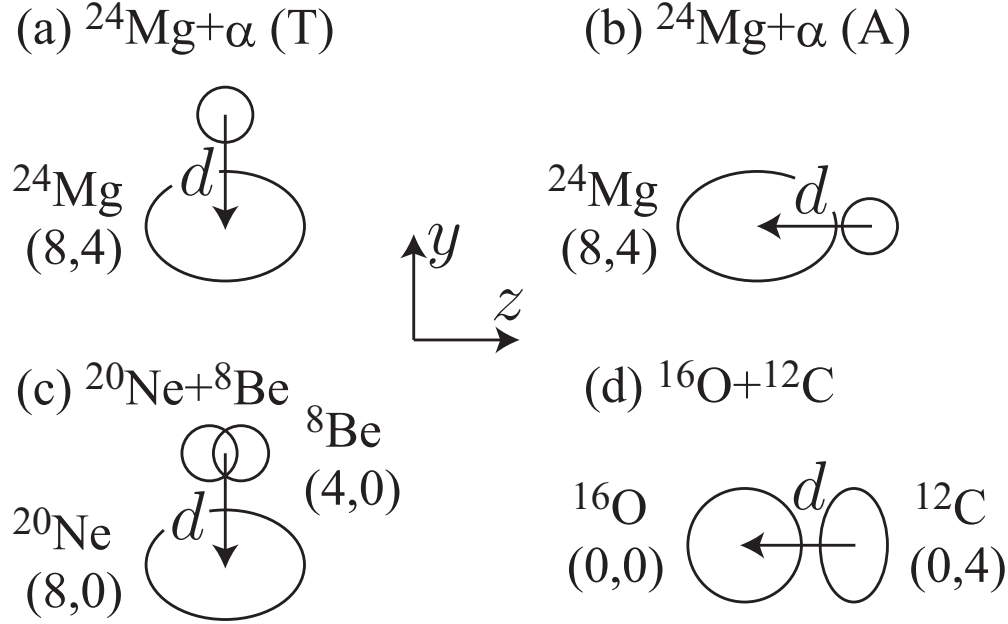


FIG. 7. Schematic figure for the various cluster configurations and their duality.

in which the orbit occupied by the last four nucleons is different from that in the ground state. The excitation of the last four nucleons into pf -shell yields the SD configuration which is given by the $(\lambda, \mu) = (20, 4)$ representation.

$$(\lambda, \mu) = (20, 4) : (002)^4(011)^4(003)^4. \quad (20)$$

The Bayman-Bohr theorem tells that these $SU(3)$ shell model wave functions are identical to the cluster model wave functions with the zero inter-cluster distance. First, we consider $^{24}\text{Mg} + \alpha$ cluster configurations. The triaxially deformed ground state of ^{24}Mg is given by the $(\lambda, \mu) = (8, 4)$ representation,

$$(\lambda, \mu) = (8, 4) : (002)^4(011)^4, \quad (21)$$

where the longest deformation axis is z -axis. Now we consider the $^{24}\text{Mg} + \alpha$ configuration in which the α cluster is placed on the y -axis as illustrated in Fig. 7 (a). This configuration corresponds to the $^{24}\text{Mg} + \alpha$ (T) configuration obtained by AMD calculation. Since the orbits (000) and (010) are already occupied by the nucleons in ^{24}Mg cluster, the nucleons in the α cluster having (000)⁴ configuration must occupy (020)⁴ at zero inter-cluster distance $d = 0$. As a result, one sees that the $^{24}\text{Mg} + \alpha$ (T) cluster configuration becomes identical

to the $(0, 12)$ representation for the ground state given by Eq. (19),

$$\lim_{d \rightarrow 0} \Phi_{24\text{Mg}+\alpha(\text{T})}(d) = (002)^4(011)^4(020)^4. \quad (22)$$

This clearly explains why the $^{24}\text{Mg} + \alpha$ (T) configuration obtained by the d -constraint becomes almost identical to the ground state configuration at small inter-cluster distance d . The placement of the α particle on z -axis corresponds the another configuration $^{24}\text{Mg} + \alpha$ (A) as shown in Fig. 7 (b). In this case, at zero inter-cluster distance, the nucleons in the α cluster occupy $(003)^4$ resulting in the SD configuration given by Eq. (20),

$$\lim_{d \rightarrow 0} \Phi_{24\text{Mg}+\alpha(\text{A})}(d) = (002)^4(011)^4(003)^4. \quad (23)$$

The other cluster configurations are also considered in the same way. The prolately deformed ground state of ^{20}Ne is given by the $(\lambda, \mu) = (8, 0)$ representation,

$$(\lambda, \mu) = (8, 0) : (002)^4, \quad (24)$$

where the symmetry axis of ^{20}Ne is z -axis. The $^{20}\text{Ne} + ^8\text{Be}$ configuration corresponds to the placement of ^8Be cluster on y -axis where the symmetry axis of ^8Be is also z -axis (Fig. 7 (c)). At zero inter-cluster distance, the nucleons in the ^8Be cluster having $(000)^4(001)^4$ configuration occupy $(020)^4(011)^4$ due to the Pauli principle, and one finds it is identical to the ground state configuration,

$$\lim_{d \rightarrow 0} \Phi_{20\text{Ne}+^8\text{Be}}(d) = (002)^4(011)^4(020)^4. \quad (25)$$

The oblately deformed ground state of ^{12}C is given by the $(\lambda, \mu) = (0, 4)$ representation,

$$(\lambda, \mu) = (0, 4) : (000)^4(100)^4(010)^4, \quad (26)$$

where the symmetry axis is z -axis. The $^{16}\text{O} + ^{12}\text{C}$ configuration corresponds the placement of ^{16}O and ^{12}C clusters on z -axis as shown in Fig. 7 (d). At zero inter-cluster distance, it is identical to the prolate deformed state,

$$\lim_{d \rightarrow 0} \Phi_{16\text{O}+^{12}\text{C}}(d) = (002)^4(011)^4(101)^4. \quad (27)$$

Thus, considering the corresponding $SU(3)$ shell model wave function, the duality of the mean-field and cluster configurations illustrated in Fig. 6 is clearly explained. It is also

noted that the duality of the shell and cluster in ^{28}Si was also investigated and found by the Skyrme Hartree-Fock calculation [11].

As discussed in Refs. [40, 41, 43], this duality of shell and cluster means that the degree-of-freedom of $^{28}\text{Mg} + \alpha$ (T) and $^{20}\text{Ne} + ^8\text{Be}$ cluster excitations are embedded in the ground state. Therefore, the excitation of the inter-cluster motion embedded in the ground state yields excited cluster states with pronounced $^{24}\text{Mg} + \alpha$ (T) and $^{20}\text{Ne} + ^8\text{Be}$ configurations. The important fact is that the IS monopole and dipole transitions between the ground state and these excited cluster states are very strong, and hence, these transitions are very good probe for the clustering. Indeed, if one assumes that the ground state is a pure $SU(3)$ shell model state and the excited cluster states are described by the cluster model wave function, it is possible to analytically show the enhancement of the IS monopole and dipole transitions [40, 43]. However, in the case of ^{28}Si , the ground state deviates from a pure $SU(3)$ shell model state because of the strong influence of the spin-orbit interaction. In addition to this, the coupling between the cluster configurations and mean-field configurations in the excited states is not negligible. Therefore, the evaluation of the transition strengths by the realistic nuclear model is indispensable for the quantitative discussions. For this purpose, we present the results of the GCM calculation below.

B. Isoscalar monopole and dipole transitions

Using the wave functions of the ground and excited cluster states obtained by the GCM calculation, the IS monopole and dipole transition strengths are directly evaluated. The transition operators and matrix elements between the ground and excited states are given as,

$$\mathcal{M}(IS0) = \sum_{i=1}^A (\mathbf{r}_i - \mathbf{r}_{cm})^2, \quad (28)$$

$$\mathcal{M}_\mu(IS1) = \sum_{i=1}^A (\mathbf{r}_i - \mathbf{r}_{cm})^2 \mathcal{Y}_{1\mu}(\mathbf{r}_i - \mathbf{r}_{cm}) \quad (29)$$

$$M(IS0; 0_1^+ \rightarrow 0_n^+) = \langle 0_n^+ | \mathcal{M}(IS0) | 0_1^+ \rangle, \quad (30)$$

$$\begin{aligned} M(IS1; 0_1^+ \rightarrow 1_n^-) &= \langle 1_n^- | | \mathcal{M}_0(IS1) | | 0_1^+ \rangle \\ &= \sqrt{3} \langle 1_n^- | \mathcal{M}_0(IS1) | 0_1^+ \rangle, \end{aligned} \quad (31)$$

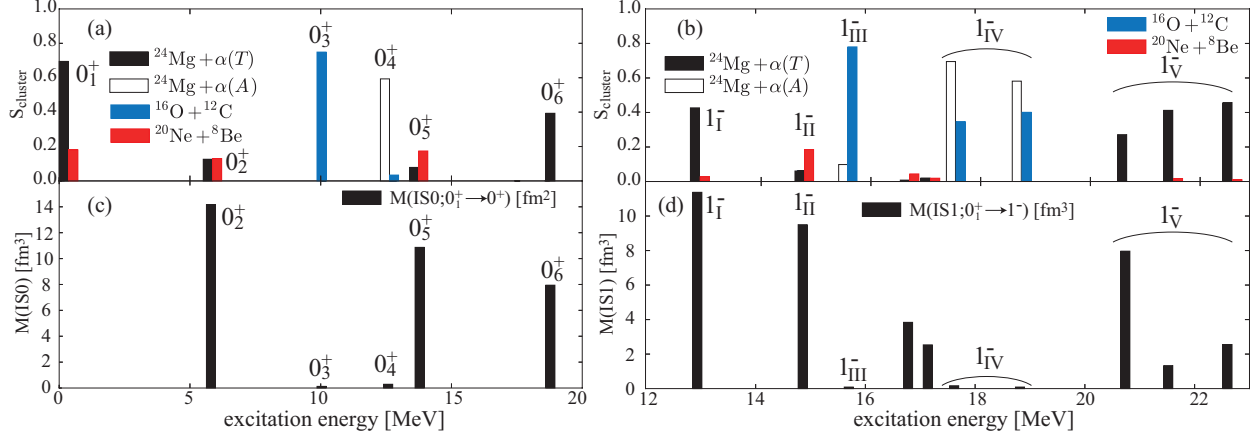


FIG. 8. (a) The cluster S -factors for the ground and excited 0^+ states. (b) Same as (a) but for the excited 1^- states. (c) The IS monopole transition matrix from the ground state to the excited 0^+ states. (d) The IS dipole transition matrix from the ground state to the excited 1^- states.

where \mathbf{r}_i and \mathbf{r}_{cm} denote the single-particle and center-of-mass coordinates, respectively. The solid spherical harmonics is defined as $\mathcal{Y}_{1\mu}(\mathbf{r}) = rY_{1\mu}(\hat{r})$. We also calculated the cluster S -factors of the ground and excited states to see how the clustering and IS monopole and dipole transitions are correlated to each other.

The results are shown in Fig. 8 where the panels (a) and (b) show the cluster S -factors of 0^+ and 1^- states, while the panels (c) and (d) shows the IS monopole and dipole transition matrices. The calculated S -factors confirm the clustering systematics summarized in Fig. 6. Owing to the duality of the shell and cluster, the ground state has large S -factor for the $^{24}\text{Mg} + \alpha(T)$ configuration which amounts to 0.68 and has non-negligible S -factor for the $^{20}\text{Ne} + ^8\text{Be}$ configuration. The 0_6^+ state is regarded as the pronounced $^{24}\text{Mg} + \alpha(T)$ cluster state, while the $0_5^+(0_2^+)$ state is regarded as the pronounced $^{20}\text{Ne} + ^8\text{Be}$ cluster states from their S -factors. One also sees that the 1_1^- state and a group of 1^- state denoted by $1_{\bar{V}}$ are the $^{24}\text{Mg} + \alpha(T)$ cluster states and paired with the ground state and the 0_6^+ state, respectively, while the 1_{II}^- state should be paired with the 0_5^+ state to constitute the $^{20}\text{Ne} + ^8\text{Be}$ doublet. In the same way, the S -factors clearly show that the 0_3^+ and 1_{III}^- states are the $^{16}\text{O} + ^{12}\text{C}$ doublet, and the 0_4^+ and 1_{IV}^- states are the $^{24}\text{Mg} + \alpha(A)$ doublet although the $^{16}\text{O} + ^{12}\text{C}$ configuration is also mixed in the 1_{IV}^- states.

It is very impressive to see that the IS monopole and dipole strengths shown in the panels (c) and (d) are very strongly correlated to the S -factors for the $^{24}\text{Mg} + \alpha(A)$ and $^{20}\text{Ne} + ^8\text{Be}$

configurations, but almost insensitive to the other cluster and non-cluster states except for a couple of 1^- states around 17 MeV. Because the IS monopole and dipole operators activate the degree-of-freedom of cluster excitation embedded in the ground state, the transition strengths to the $^{24}\text{Mg} + \alpha$ (A) and $^{20}\text{Ne} + ^8\text{Be}$ cluster states are as strong as the single-particle estimates which are given as,

$$M(IS0)_{WU} = \frac{3}{5}(1.2A^{1/3})^2 \simeq 8.0 \text{ fm}^2 \quad (32)$$

$$M(IS1)_{WU} = \sqrt{\frac{3}{16\pi}}(1.2A^{1/3})^3 \simeq 11.8 \text{ fm}^2. \quad (33)$$

Therefore, we can conclude that the IS monopole and dipole transitions are good probe to identify the $^{24}\text{Mg} + \alpha$ (T) and $^{20}\text{Ne} + ^8\text{Be}$ clustering.

Recently, an interesting and promising experimental data was reported by the measurement of the $^{28}\text{Si}(\alpha, \alpha')^{28}\text{Si}^*$ inelastic scattering [58, 59]. It was found that a couple of 0^+ states above 9 MeV are strongly populated and deduced to have large IS monopole transition strengths. Hence, they are suggested as strong candidates of the α cluster states [59]. We expect that the detailed comparison of the IS monopole and dipole transition strengths between experiment and theory will reveal the clustering systematics in ^{28}Si .

V. SUMMARY

In summary, we have investigated the clustering systematics in ^{28}Si based on the anti-symmetrized molecular dynamics. It is found that the inversion doublet bands with various kinds of reflection-asymmetric cluster configuration appears in the excited states, and the IS monopole and dipole transitions are good probe for $^{24}\text{Mg} + \alpha$ (T) and $^{20}\text{Ne} + ^8\text{Be}$ cluster states.

The energy variation by using d -constraint yielded various kinds of cluster configurations with positive- and negative-parity, while the $\beta\gamma$ -constraint yielded mean-field configurations. It is found that the cluster configurations become identical to the mean-field configurations at small inter-cluster distance because of the duality of mean-field (shell) and cluster. In particular, it is emphasized that the oblate deformed ground state has the duality of the $^{24}\text{Mg} + \alpha$ (T) and $^{20}\text{Ne} + ^8\text{Be}$ configurations.

The GCM calculation showed that a group of the $^{24}\text{Mg} + \alpha$ (T) and $^{20}\text{Ne} + ^8\text{Be}$ cluster bands are generated by the excitation of the inter-cluster motion embedded in the ground

state. In addition to them, the prolate and SD bands have the duality of $^{16}\text{O}+^{12}\text{C}$ and $^{20}\text{Ne}+^8\text{Be}$ clustering, respectively. Because of their reflection-asymmetric intrinsic configurations, they are accompanied by the negative-parity bands to constitute the inversion doublets.

Because of the duality of the ground state, it is numerically shown that the $^{24}\text{Mg} + \alpha$ (T) and $^{20}\text{Ne} + ^8\text{Be}$ cluster bands have enhanced IS monopole and dipole transition matrices which are as large as the single-particle estimates. On the other hand, other cluster states and non-cluster states are rather insensitive to the IS monopole and dipole transitions. Hence, we conclude that the $^{24}\text{Mg} + \alpha$ (T) and $^{20}\text{Ne} + ^8\text{Be}$ cluster bands can be identified from their enhanced transitions. We expect that more quantitative comparison with the experiments will reveal the clustering systematics in ^{28}Si .

ACKNOWLEDGMENTS

The authors thanks to Prof. Kanada-En'yo and Prof. Kawabata and Prof. Ito for the fruitful discussions. Part of the numerical calculations were performed by using the supercomputers at the High Energy Accelerator Research Organization (KEK) and at Yukawa Institute for Theoretical Physics (YITP) in Kyoto University. The support by the Grants-in-Aid for Scientific Research on Innovative Areas from MEXT (Grant No. 2404:24105008) and JSPS KAKENHI Grant Nos. 16J03654, 25800124 and 16K05339 are acknowledged.

-
- [1] Y. Fujiwara, H. Horiuchi, K. Ikeda, M. Kamimura, K. Kato, Y. Suzuki, and E. Uegaki, *Prog. Theor. Phys. Suppl.* **68**, 29 (1980).
 - [2] M. Kimura and H. Horiuchi, *Phys. Rev. C* **69**, 051304 (2004).
 - [3] M. Kimura, *Phys. Rev. C* **69**, 044319 (2004).
 - [4] Y. Taniguchi, Y. Kanada-En'yo, and M. Kimura, *Phys. Rev. C* **80**, 044316 (2009).
 - [5] S. Das Gupta and M. Harvey, *Nucl. Phys. A* **94**, 602 (1967).
 - [6] F. Glatz, P. Betz, J. Siefert, F. Heindinger, and H. Röpke, *Phys. Rev. Lett.* **46**, 1559 (1981).
 - [7] F. Glatz, J. Siefert, P. Betz, E. Bitterwolf, A. Burkard, F. Heindinger, T. Kern, R. Lehmann, S. Norbert, and H. Röpke, *Zeitschrift Phys. A Atoms Nucl.* **303**, 239 (1981).
 - [8] R. K. Sheline, S. Kubono, K. Morita, and M. Tanaka, *Phys. Lett. B* **119**, 263 (1982).

- [9] J. Cseh and W. Scheid, *J. Phys. G Nucl. Part. Phys.* **18**, 1419 (1992).
- [10] S. Ohkubo and K. Yamashita, “Parity-doublet $16\text{O}+12\text{C}$ cluster bands in 28Si ,” (2004).
- [11] J. A. Maruhn, M. Kimura, S. Schramm, P.-G. Reinhard, H. Horiuchi, and A. Tohsaki, *Phys. Rev. C* **74**, 044311 (2006).
- [12] T. Ichikawa, Y. Kanada-En’yo, and P. Möller, *Phys. Rev. C* **83**, 054319 (2011).
- [13] J. Darai, J. Cseh, and D. G. Jenkins, *Phys. Rev. C* **86**, 064309 (2012).
- [14] J. J. Kolata, R. A. Kryger, P. A. DeYoung, and F. W. Prosser, *Phys. Rev. Lett.* **61**, 1178 (1988).
- [15] C. Beck, F. Haas, R. Freeman, B. Heusch, J. Coffin, G. Guillaume, F. Rami, and P. Wagner, *Nucl. Phys. A* **442**, 320 (1985).
- [16] M. A. Eswaran, S. Kumar, E. T. Mirgule, D. R. Chakrabarty, V. M. Datar, N. L. Ragoowansi, and U. K. Pal, *Phys. Rev. C* **47**, 1418 (1993).
- [17] D. G. Jenkins, C. J. Lister, M. P. Carpenter, P. Chowdury, N. J. Hammond, R. V. F. Janssens, T. L. Khoo, T. Lauritsen, D. Seweryniak, T. Davinson, P. J. Woods, A. Jokinen, H. Penttila, F. Haas, and S. Courtin, *Phys. Rev. C* **86**, 064308 (2012).
- [18] J. Maas, E. Somorjai, H. Graber, C. Van Den Wijngaart, C. Van Der Leun, and P. Endt, *Nucl. Phys. A* **301**, 213 (1978).
- [19] J. Cseh, E. Koltay, Z. Máté, E. Somorjai, and L. Zolnai, *Nucl. Phys. A* **385**, 43 (1982).
- [20] T. Tanabe, K. Haga, M. Yasue, K. Sato, K. Ogino, Y. Kadota, M. Tochi, K. Makino, T. Kitahara, and T. Shiba, *Nucl. Phys. A* **399**, 241 (1983).
- [21] S. Kubono, K. Morita, M. Tanaka, A. Sakaguchi, M. Sugitani, and S. Kato, *Nucl. Phys. A* **457**, 461 (1986).
- [22] K. P. Artemov, M. S. Golovkov, V. Z. Goldberg, V. I. Dukhanov, I. B. Mazurov, V. V. Pankratov, V. V. Paramonov, V. P. Rudakov, I. N. Serikov, V. A. Solovev, and V. A. Timofeev, *Sov. J. Nucl. Phys.* **51**, 777 (1990).
- [23] R. Stokstad, D. Shapira, L. Chua, P. Parker, M. W. Sachs, R. Wieland, and D. A. Bromley, *Phys. Rev. Lett.* **28**, 1523 (1972).
- [24] H. Fröhlich, P. Dück, W. Galster, W. Treu, H. Voit, H. Witt, W. Kühn, and S. Lee, *Phys. Lett. B* **64**, 408 (1976).
- [25] P. Charles, F. Auger, I. Badawy, B. Berthier, M. Dost, J. Gastebois, B. Fernandez, S. Lee, and E. Plagnol, *Phys. Lett. B* **62**, 289 (1976).

- [26] D. James, G. Morgan, N. Fletcher, and M. Greenfield, Nucl. Phys. A **274**, 177 (1976).
- [27] M. Shawcross, N. Curtis, W. N. Catford, N. M. Clarke, B. R. Fulton, S. J. Hall, J. T. Murgatroyd, S. P. G. Chappell, R. L. Cowin, G. Dillon, and D. L. Watson, Phys. Rev. C **63**, 034311 (2001).
- [28] N. I. Ashwood, J. T. Murgatroyd, N. M. Clarke, M. Freer, B. R. Fulton, A. St. J. Murphy, S. P. G. Chappell, R. L. Cowin, G. K. Dillon, D. L. Watson, W. N. Catford, N. Curtis, M. Shawcross, and V. Pucknell, Phys. Rev. C **63**, 034315 (2001).
- [29] A. Goasduff, S. Courtin, F. Haas, D. Lehbertz, D. G. Jenkins, J. Fallis, C. Ruiz, D. A. Hutcheon, P.-A. Amandruz, C. Davis, U. Hager, D. Ottewell, and G. Ruprecht, Phys. Rev. C **89**, 014305 (2014).
- [30] D. Baye, Nucl. Phys. A **272**, 445 (1976).
- [31] D. Baye and P.-H. Heenen, Nucl. Phys. A **283**, 176 (1977).
- [32] K. Kato, S. Okabe, and Y. Abe, Prog. Theor. Phys. **74**, 1053 (1985).
- [33] Y. Kondo and M. Katsuma, Nucl. Phys. A **738**, 226 (2004).
- [34] J. Cseh, Phys. Rev. C **27**, 2991 (1983).
- [35] P. O. Hess, A. Algora, J. Cseh, and J. P. Draayer, Phys. Rev. C **70**, 051303 (2004).
- [36] H. Horiuchi and K. Ikeda, Prog. Theor. Phys. **40**, 277 (1968).
- [37] Y. Suzuki, Nucl. Phys. A **470**, 119 (1987).
- [38] T. Kawabata, H. Akimune, H. Fujita, Y. Fujita, M. Fujiwara, K. Hara, K. Hatanaka, M. Itoh, Y. Kanada-En'yo, S. Kishi, K. Nakanishi, H. Sakaguchi, Y. Shimbara, A. Tamii, S. Terashima, M. Uchida, T. Wakasa, Y. Yasuda, H. Yoshida, and M. Yosoi, “ $2\alpha+t$ cluster structure in 11B ,” (2007).
- [39] Y. Kanada-En'yo, Phys. Rev. C **75**, 024302 (2007).
- [40] T. Yamada, Y. Funaki, H. Horiuchi, K. Ikeda, and A. Tohsaki, Prog. Theor. Phys. **120**, 1139 (2008).
- [41] H. Horiuchi, K. Ikeda, and K. Kato, Prog. Theor. Phys. Suppl. **192**, 1 (2012).
- [42] Y. Chiba and M. Kimura, Phys. Rev. C **91**, 061302 (2015).
- [43] Y. Chiba, M. Kimura, and Y. Taniguchi, Phys. Rev. C **93**, 034319 (2016).
- [44] J. P. Elliott, Proc. R. Soc. London A Math. Phys. Eng. Sci. **245** (1958).
- [45] J. P. Elliott, Proc. R. Soc. London A Math. Phys. Eng. Sci. **245** (1958).
- [46] Y. Kanada-En'yo, M. Kimura, and H. Horiuchi, Comptes Rendus Phys. **4**, 497 (2003).

- [47] Y. Kanada-En'yo and M. Kimura, in *Lect. Notes Phys.*, Vol. 818 (Springer Berlin Heidelberg, 2010) pp. 129–164.
- [48] Y. Kanada-En'yo, M. Kimura, and A. Ono, *Prog. Theor. Exp. Phys.* **2012**, 1A202 (2012).
- [49] J. Berger, M. Girod, and D. Gogny, *Comput. Phys. Commun.* **63**, 365 (1991).
- [50] M. Kimura, R. Yoshida, and M. Isaka, *Prog. Theor. Phys.* **127**, 287 (2012).
- [51] Y. Taniguchi, M. Kimura, and H. Horiuchi, *Prog. Theor. Phys.* **112**, 475 (2004).
- [52] Y. Taniguchi, M. Kimura, Y. Kanada-En'yo, and H. Horiuchi, *Phys. Rev. C* **76**, 044317 (2007).
- [53] Y. Taniguchi, *Prog. Theor. Exp. Phys.* **2014**, 73D01 (2014).
- [54] D. L. Hill and J. A. Wheeler, *Phys. Rev.* **89**, 1102 (1953).
- [55] J. J. Griffin and J. A. Wheeler, *Phys. Rev.* **108**, 311 (1957).
- [56] J. K. Perring, T. H. R. Skyrme, A. F. T. Lauritsen, D. D. M. G. G. Devons S, L. G. R, E. J. P. R, S. T. H, and W. D. H, *Proc. Phys. Soc. Sect. A* **69**, 600 (1956).
- [57] B. Bayman and A. Bohr, *Nucl. Phys.* **9**, 596 (1958).
- [58] T. Peach, U. Garg, Y. K. Gupta, J. Hoffman, J. T. Matta, D. Patel, P. V. M. Rao, K. Yoshida, M. Itoh, M. Fujiwara, K. Hara, H. Hashimoto, K. Nakanishi, M. Yosoi, H. Sakaguchi, S. Terashima, S. Kishi, T. Murakami, M. Uchida, Y. Yasuda, H. Akimune, T. Kawabata, M. N. Harakeh, and G. Colò, *Phys. Rev. C* **93**, 064325 (2016).
- [59] P. Adsley, D. G. Jenkins, J. Cseh, S. S. Dimitriova, J. W. Brümmer, K. C. W. Li, D. J. Marín-Lámbarri, K. Lukyanov, N. Y. Kheswa, R. Neveling, P. Papka, L. Pellegri, V. Pesudo, L. C. Pool, G. Riczu, F. D. Smit, J. J. van Zyl, and E. Zemlyanaya, (2016), arXiv:1609.00296.